
1 **Biomass burning emissions of black carbon over the Maritime**
2 **Continent and ENSO variability**
3

4 Biyin Xie,^a Yang Yang,^a Hailong Wang,^b Pinya Wang,^a Hong Liao^a
5

6 ^a*Joint International Research Laboratory of Climate and Environment Change (ILCEC), Jiangsu Key*
7 *Laboratory of Atmospheric Environment Monitoring and Pollution Control, Jiangsu Collaborative Innovation*
8 *Center of Atmospheric Environment and Equipment Technology, School of Environmental Science and*
9 *Engineering, Nanjing University of Information Science and Technology, Nanjing, Jiangsu, China*

10 ^b*Atmospheric Sciences and Global Change Division, Pacific Northwest National Laboratory, Richland,*
11 *Washington, USA*

12

13 *Corresponding author: Yang Yang, yang.yang@nuist.edu.cn*

15 Fire emissions from the Maritime Continent (MC) over the western tropical Pacific are
16 strongly influenced by El Niño–Southern Oscillation (ENSO), posing various climate effect to
17 the Earth system. In this study, we show that the historical biomass burning emissions of black
18 carbon (BC_{bb}) aerosol in the dry season from the MC are strengthened in El Niño years due to
19 the dry conditions. The Eastern-Pacific type of El Niño exerts a stronger modulation in BC_{bb}
20 emissions over the MC region than the Central-Pacific type of El Niño. Based on simulations
21 using the fully coupled Community Earth System Model (CESM), the impacts of increased
22 BC_{bb} emissions on ENSO variability and frequency are also investigated in this study. With
23 BC_{bb} emissions from the MC scaled up by a factor of 10, which enables the identification of
24 climate response from the internal variability, the increased BC_{bb} heats the local atmosphere
25 and changes land-sea thermal contrast, which suppresses the westward transport of the eastern
26 Pacific surface water. It leads to an increase of sea surface temperature in the eastern tropical
27 Pacific, which further enhances ENSO variability and increases the frequency of extreme El
28 Niño and La Niña events. This study highlights the potential role of BC_{bb} emissions on extreme
29 ENSO frequency and this role may be increasingly important in the warming future with higher
30 wildfire risks.

31 1. Introduction

32 El Niño–Southern Oscillation (ENSO) is the strongest interannual climate variation signal
33 globally. It is characterized by anomalous sea surface temperature (SST) in the central-to-
34 eastern tropical Pacific, oscillating irregularly between its warm (El Niño) and cold (La Niña)
35 phases. These SST anomalies can alter atmospheric circulations and arouse teleconnection
36 patterns (Bjerknes, 1969), which exert pronounced global impacts on social stability and
37 economic growth through modulating crop yields (Iizumi et al., 2014), drought and flood
38 hazards (Jiménez-Muñoz et al., 2016; Ward et al., 2016), heat waves and cold surges
39 (Thirumalai et al., 2017), tropical cyclones (Sobel and Maloney, 2000), and ice melting in polar
40 regions (Hu et al., 2016; Nicolas et al., 2017).

41 The Maritime Continent (MC) is the western boundary of the tropical Pacific under the
42 ascending branch of the Walker Circulation, which is susceptible to ENSO-related circulation
43 changes. During the developing phase of El Niño, precipitation over the MC is suppressed,
44 reducing the wet deposition of aerosols and promoting dry conditions favorable for fire burning
45 (Chen et al., 2017; Wu et al., 2013). The severest fire years of the MC in the past few decades,
46 such as 1991, 1997 and 2015, are all El Niño years (van Marle et al., 2017). Fire emissions
47 during the major fire season of equatorial Asia were nearly tenfold higher during El Niño years
48 than during La Niña years (Chen et al., 2017). In recent decades, biomass burning has become
49 more frequent and widespread across the MC due to human activities, including land clearing,
50 land-use change, poor peatland management, and burning of agriculture waste (Dennis et al.,
51 2005; Marlier et al., 2015a; Lee et al., 2017). Large-scale and high-emission biomass burning
52 activities occur every year in the dry season that usually peaks from August/September to
53 October/November. Based on economic incentives and population growth in Southeast Asia,
54 future land-use management will play an important role in determining fire activities across the
55 region (Carlson et al., 2012; Marlier et al., 2015b). Furthermore, climate warming will generally
56 increase the risk of fire and can also affect the fire injection and plume height (Szopa et al.,
57 2021), which indicates that aerosol emissions from wildfire will increase in the future.

58 Changes in biomass burning aerosols over the MC could influence regional climate change.
59 Biomass burning aerosols from fire emissions during El Niño events heat the middle and upper

60 troposphere and cool the surface, thus increase static stability near the surface. The increased
61 stability together with reduced specific humidity and weakened surface convergence suppress
62 convection and precipitation, exacerbating drought in the source region of the MC (Tosca et al.,
63 2010). During the extreme El Niño of 1997, carbonaceous aerosols from the Indonesian fires
64 induced radiative forcings at the surface by about -10 W m^{-2} over most of the tropical Indian
65 Ocean and -150 W m^{-2} over the burning regions (Duncan et al., 2003).

66 Black carbon (BC) is an important component of aerosols emitted from incomplete
67 combustion. Globally, open biomass burning account for about 15% of the total BC emissions.
68 Long-term measurements in Indonesia (Rashid et al., 2014; Sattar et al., 2014) revealed that BC
69 was elevated during the dry season because of the biomass burning emissions and relatively
70 low rainfall. BC has diverse impacts on meteorology and climate by directly absorbing solar
71 radiation within the atmospheric column, affecting cloud formation and lifetime, and reducing
72 surface albedo through deposition on snow and ice (McFarquhar and Wang, 2006; Ramanathan
73 and Carmichael, 2008; Kang et al., 2020). The influence of heating effect of BC aerosols in the
74 atmosphere depends on its vertical position. The BC-induced heating aloft increases stability
75 below the BC layer and enhances vertical motion above the BC layer (Stocker et al., 2013). The
76 warming effect of BC can be enhanced by coating its surface with organic carbon (OC), which
77 leads to the “lensing effect” where photons are focused on the BC core (Lack and Cappa, 2010).
78 Compared to fossil fuel BC (BC_{ff}) emissions, biomass burning BC (BC_{bb}) is generally
79 accompanied by higher emissions of OC, with a typical OC/BC ratio of 2 in urban traffic
80 environments and a ratio of 5 or higher in regions with prevalent biomass burning emissions
81 and smoldering dominance (Novakov et al., 2005). Also, BC_{bb} tends to be larger in size with
82 thicker coatings compared to BC_{ff} in urban environments (Schwarz et al., 2008). Based on these
83 characteristics, BC can exert significant climatic and dynamic impacts over the tropical Pacific
84 and surrounding continents by changing atmospheric vertical motion, circulation and
85 convection. Increased BC emissions in the mid-latitudes of the Northern Hemisphere and Arctic
86 could increase the frequency of extreme ENSO events through altering meridional heat
87 transport from equator to polar regions (Lou et al., 2019a). The direct radiative forcing of global
88 BC can exert precipitation change pattern similar to that corresponding to ENSO activities
89 (Wang, 2007). BC from biomass burning and industrial emissions from Indo-Gangetic Plain is

90 also able to amplify the effect of ENSO on the Indian summer monsoon (Kim et al., 2016).

91 Previous studies have shown that the intensity and frequency of ENSO events might
92 increase under climate warming (Stevenson, 2012; Cai et al., 2014, 2015, 2018; Wang et al.,
93 2018; Wang B. et al., 2019). Many studies have reported that aerosols and their precursor gases
94 can affect ENSO properties, including its intensity, frequency and duration. Fasullo et al. (2023)
95 identified that 2019-2020 Australian wildfires caused a significant increase in biomass aerosol
96 burdens, altered cloud properties, and led to cooling in the tropical Pacific Ocean, ultimately
97 contributing to the occurrence of strong La Niña events in 2020-2022. Using simulations of
98 global climate models, Yang et al. (2016a, b) found a positive sea salt emission-ENSO feedback,
99 in which changes in sea salt emissions enhance the variability of ENSO. Xu and Yu (2019)
100 investigated the ENSO-induced aerosol dipole over the International Dateline and the MC
101 regions and proposed a positive feedback of aerosol dipole pattern to ENSO evolution. Several
102 other studies found that stratospheric sulfate aerosols, formed from sulfur dioxide (SO_2)
103 injected by tropical volcanic eruptions, influence the ENSO through changing the earth
104 radiation budget (Wang et al., 2018; Ward et al., 2021). How the increasing BC_{bb} from the MC
105 potentially influences ENSO variability remains unexplored.

106 In this study, we show that the boreal winter mean Niño indices are positively correlated
107 with the preceding September-October-November (SON) BC_{bb} emissions over the MC based
108 on a long-term statistical analysis and analyze meteorological parameters leading to the increase
109 of BC_{bb} emissions associated with El Niño. Then the mechanism of the substantial increase in
110 year-round BC_{bb} emissions from the MC regulating ENSO variability is identified based on
111 long-term global aerosol-climate model simulations. The model, simulations, and observational
112 datasets are described in Section 2. The impacts of BC from the MC on ENSO variability and
113 the potential mechanisms are analyzed in Section 3. These results are summarized and discussed
114 in Section 4.

115

116 **2. Methods**

117 *a. Data*

118 The meteorological and aerosol emission datasets used in this study include the following:

119 1. For biomass burning emissions, we utilize the BB4CMIP dataset (available at
120 <https://esgf-node.llnl.gov/search/input4mips/>; van Marle et al., 2017). BB4CMIP combines
121 satellite-observed fire emissions with regional proxy datasets and modeled data to provide a
122 global estimation of emissions of various aerosols and gases at a horizontal resolution of
123 $0.25^\circ \times 0.25^\circ$ and covers the period from 1750 to 2015 for Coupled Model Inter-comparison
124 Project phase 6 (CMIP6). This dataset divides the world into 17 regions with different data
125 sources. For the MC region in this study, the biomass burning emission data primarily originate
126 from the Equatorial Asia (EQAS) region within BB4CMIP. In the EQAS region, the emission
127 data from 1997 to 2015 are based on the Global Fire Emissions Database version 4 with small
128 fires (GFED4s). The emission data from 1950 to 1996 are based on visibility observations from
129 the World Meteorological Organization (WMO) stations in the EQAS. However, the emission
130 data from 1750 to 1949 are held constant at the lowest decadal average (van Marle et al., 2017).
131 Therefore, in the EQAS region of BB4CMIP, the data from 1950 to 2015 are considered more
132 reliable compared to the earlier period. In this study, for historical data analysis, we use
133 BB4CMIP data from 1950 to 2015. For model input, we use data of 2006 that are regridded to
134 0.9° (latitude) $\times 1.25^\circ$ (longitude) and divided into 13 levels.

135 2. For calculation of historical Niño indices, we utilize monthly sea surface temperature
136 from the NOAA Extended Reconstructed SST V5 (ERSST v5; available at
137 <https://psl.noaa.gov/data/gridded/data.noaa.ersst.v5.html>) with a horizontal resolution of $2^\circ \times 2^\circ$
138 from 1950 to 2016.

139 3. For historical analysis of meteorological conditions for increasing BC_{bb} from the MC
140 region during El Niño, we utilize monthly mean meteorological fields (i.e., sea level pressure,
141 winds) from ERA5 reanalysis (available at <https://cds.climate.copernicus.eu/>; Hersbach et al.,
142 2020) with a horizontal resolution of $0.25^\circ \times 0.25^\circ$ from 1979 to 2015 and monthly mean
143 precipitation from the Global Precipitation Climatology Project (GPCP; available at
144 <https://www.ncei.noaa.gov/data/global-precipitation-climatology-project-gpcp-monthly/access/>; Adler et al., 2018) with a horizontal resolution of $2.5^\circ \times 2.5^\circ$ from 1979 to
145 2015.

147 4. For anthropogenic emissions of model input, we use the Community Emissions Data
148 System (CEDS; available at <https://esgf-node.llnl.gov/search/input4mips/>; Hoesly et al., 2018).

149 Specifically, we use CEDS emissions of BC, OC, SO₂, and volatile organic compounds (VOCs)
150 from various anthropogenic sectors in year 2006. The CEDS emissions originally have a spatial
151 resolution of 0.5° and are regridded to a resolution of 0.9° (latitude) × 1.25° (longitude) for our
152 analysis and model simulation.

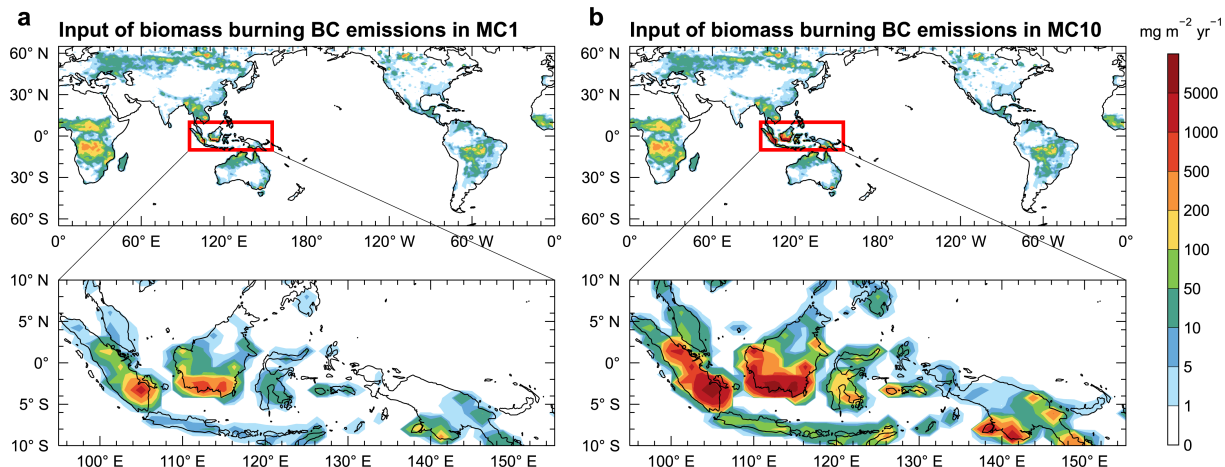
153

154 *b. Model configuration*

155 In this study, simulations are performed with the coupled global aerosol-climate model,
156 Community Earth System Model version 1.2 (CESM1.2; Hurrell et al., 2013), which has been
157 widely used to quantify aerosol-climate interactions (Yang et al., 2017, 2019, 2023; Lou et al.,
158 2019a, b). The atmospheric component of CESM is the Community Atmosphere Model version
159 5.3 (CAM5.3) configured with a 1.9° (latitude) × 2.5° (longitude) horizontal resolution and 30
160 vertical levels, in which mass and number concentrations of aerosols (including sulfate [SO₄²⁻],
161 BC, primary organic matter [POM], secondary organic aerosol [SOA], mineral dust, and sea
162 salt) are represented using the four-mode (i.e., Aitken, accumulation, coarse, and primary
163 carbon modes) Modal Aerosol Module (MAM4; Liu et al., 2016). MAM4 is chosen for its aging
164 processes of primary carbonaceous aerosols that can well represent the BC aerosol lifecycle.
165 The CAM5.3 model includes aerosol-radiation interaction in shortwave and longwave bands as
166 well as aerosol-cloud interactions for stratiform clouds (Liu et al., 2012). In our model
167 simulations, to estimate the direct radiative forcing (DRF) of BC, atmospheric radiation
168 calculation is performed twice with BC included and excluded, respectively, in the estimate of
169 bulk aerosol properties for the radiative transfer model. The ocean component is the Parallel
170 Ocean Program version 2 (POP2) configured with the nominal grid gx1v6 (horizontal
171 resolution of approximately 1°) and with 60 vertical levels.

172 To assess the impact of BC_{bb} on ENSO variability, two experiments are conducted, namely
173 “MC1” and “MC10”, both of which are initialized with the same atmosphere and ocean
174 conditions at present-day levels. In the MC1 experiment, solar radiation, greenhouse gases
175 concentration, aerosol and precursor emissions are all fixed at year 2006 level with monthly
176 variations, while in the MC10 case, BC_{bb} emissions of each month over the MC (95° E–155°
177 E, 10° S–10° N) are scaled up by a factor of 10 and other regions are kept the same as MC1.
178 The reason for choosing emissions in year 2006 as the baseline is that biomass burning aerosols

179 over the MC are significantly affected by a moderate El Niño in 2006 (Chandra et al., 2009).
 180 Therefore, the emissions in 2006 are relative higher than normal but not too extreme compared
 181 to strong El Niño years (Fig. S1), which helps to distinguish the climate response signals from
 182 the internal variability. The input of BC_{bb} emissions in MC1 and MC10 are shown in Fig. 1.
 183 The large increase (i.e., the factor of 10) is used in MC10 so that climate response signals are
 184 stronger than internal variability in the climate model, which has been widely used in previous
 185 aerosol perturbation experiments (e.g., Lou et al., 2019a, b; Sand et al., 2013, 2015; Stjern et
 186 al., 2017; Yang et al., 2019). MC1 and MC10 cases are initialized with the same present-day
 187 default initial condition. For each experiment, one 135-year simulation is performed with the
 188 last 100 years used for model analysis and the first 35 years treated as model spin-up time.



189 **Fig. 1.** Annual mean biomass burning black carbon emission rate ($\text{mg m}^{-2} \text{ yr}^{-1}$) in **a** MC1 and **b** MC10
 190 simulations. The red box marks the Maritime Continent (95° E – 155° E , 10° S – 10° N). Biomass burning black
 191 carbon emission data are from the year 2006 of the BB4CMIP dataset.
 192

193

194 *c. Model evaluation*

195 We compare the global patterns and seasonal variations over the MC between
 196 reanalyzed/satellite data and simulated results. The simulated absorption aerosol optical depth
 197 of BC (AAODBC) from the MC1 case is contrasted with the reanalysis data of MERRA2
 198 (M2TMNXAER) (Fig. S2), revealing an underestimation of AAODBC over the MC region by
 199 the model. This may be attributed to the bias in BC aerosol simulation related to many factors
 200 including emissions and wet scavenging, as well as the bias in satellite retrievals related to
 201 abundance of clouds over the MC region. Remarkably, the simulated total cloud fraction

202 demonstrated a strong correspondence with the MODIS satellite data (Fig. S3). Additionally,
203 the simulated precipitation rate (Fig. S4) closely resembled the magnitude observed in the
204 GPCP reanalysis data. However, it is noteworthy that CESM1.2, like many climate models,
205 exhibited a tendency to simulate a double Intertropical Convergence Zone (ITCZ) rather than
206 the conventional single band. Also, the 2-degree version of CESM1.2 tends to simulate more
207 extreme ENSO events than those in the real world (Lou et al., 2019a).

208

209 *d. ENSO indices and statistical methods*

210 The intensity of ENSO condition is usually characterized by monthly Niño indices,
211 including Niño1+2, Niño3, Niño3.4 and Niño4 indices which are defined as the regionally
212 averaged SST anomalies over the Niño1+2 region (90° W– 80° W, 10° S– 0°), Niño3 region (150°
213 W– 90° W, 5° S– 5° N), Niño3.4 region (170° W– 120° W, 5° S– 5° N) and Niño4 region (160°
214 E– 150° W, 5° S– 5° N), respectively. The Niño indices are calculated from ERSST v5 and used
215 for the selection of historical El Niño years and the correlation analysis.

216 An El Niño (La Niña) event is usually identified based on Niño3.4 index. In the section of
217 the impact of El Niño on BC_{bb} emissions from the MC, El Niño years during 1950–2015 are
218 identified using Niño3.4 index according to the method used by the Climate Prediction Center
219 (CPC) of NOAA. Firstly, the interannual linear trend from 1950 to 2016 is removed from the
220 monthly averaged SST in the Niño3.4 region. Then, the anomalies of Niño3.4 SST removed the
221 seasonal variations are calculated. A consecutive 5-month moving average exceeding 0.5°C is
222 considered as an El Niño event. The selected El Niño years during 1950–2015 are 1951, 1953,
223 1957, 1963, 1965, 1968, 1969, 1972, 1976, 1977, 1982, 1986, 1987, 1991, 1994, 1997, 2002,
224 2004, 2006, 2009 and 2015. In the section of the impact of BC_{bb} emissions from the MC on
225 ENSO, we use the standard of Santoso et al. (2017) to identify extreme El Niño/La Niña events
226 in the model results. If the Niño3.4 SST anomalies of November–December–January, i.e., NDJ
227 (or December–January–February, i.e., DJF) exceed 1 standard deviation of Niño3.4 SST
228 anomalies of NDJ (or DJF) in MC1, it is classified as an extreme El Niño/La Niña event. The
229 standard deviation of NDJ (DJF) in MC1 is 2.1 (2.0) $^{\circ}\text{C}$.

230 The statistical significance of changes in the occurrence frequency of ENSO conditions
231 between the two simulations are tested in two steps. We first construct a Kolmogorov–Smirnov

232 test to examine whether the frequency distribution of Niño3.4 index from MC10 differs from
233 that of MC1. Next, SST data obtained from a 1400-year CESM preindustrial simulation are
234 used as a baseline to examine whether the frequency within a specific interval has changed in
235 MC10 compared to MC1. Specifically, we construct a probability distribution function (PDF)
236 for each 1-K interval of the monthly Niño3.4 index using 1000 random samples of consecutive
237 1200-month results from the 1400-year CESM control simulation with a Monte Carlo method.
238 Within each 1-K interval, if the difference between MC1 and MC10 is greater than the 95th
239 percentile or less than the 5th percentile of the PDF, the change in the Niño3.4 index distribution
240 of the interval is considered significant. However, we note that the statistical analysis based on
241 a preindustrial simulation could overestimate the significance of the ENSO differences between
242 MC1 and MC10, since that the preindustrial simulation has a weaker SST variability than
243 MC1/MC10 (Table S1). Also, the preindustrial simulation is performed using CESM version
244 1.1 (Text S1), which is the prior version of CESM1.2 for MC1 and MC10 simulations. However,
245 the two model versions share very similar ENSO statistics and should not affect the results in
246 this study.

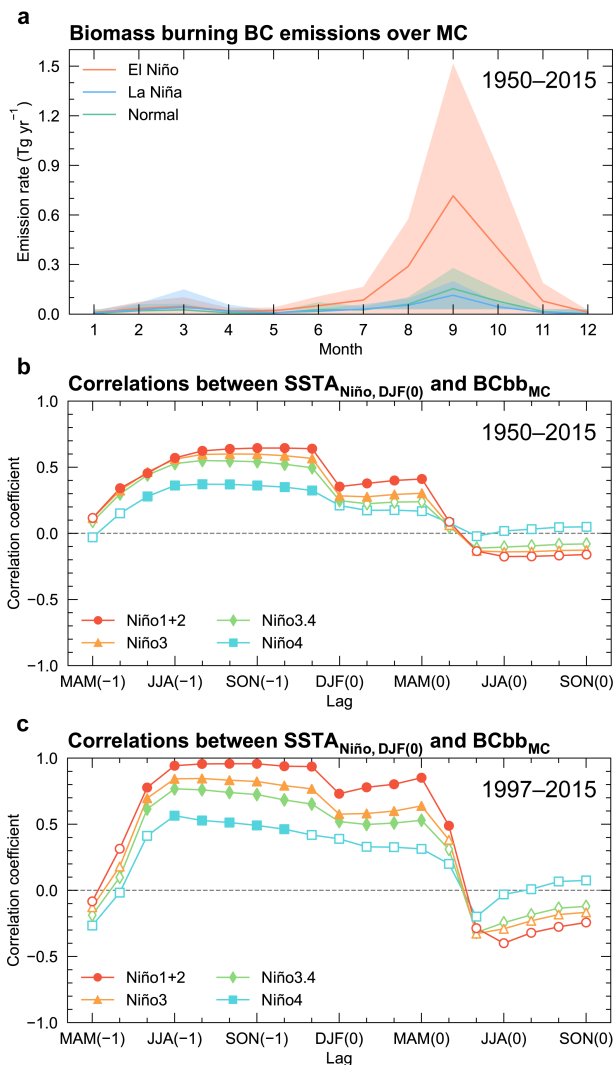
247

248 **3. Results**

249 *a. Impact of ENSO on fire emissions of BC over the Maritime Continent*

250 From the perspective of the annual cycle, BC_{bb} emission rate over the MC peaks in the late
251 boreal summer and boreal fall seasons and the emissions increase during the El Niño years (Fig.
252 2a). ENSO events usually reach their peak intensity during boreal winter. To examine whether
253 BC_{bb} emissions over the MC change with the ENSO phase and intensity, the lead-lag correlation
254 coefficients between the DJF mean Niño indices and the BC_{bb} emission rate over the MC in the
255 preceding and following seasons during 1950–2015 are calculated and shown in Fig. 2b. The
256 BC_{bb} emission rate over the MC in the fall season preceding the boreal winter of the mature
257 phase of ENSO events is positively correlated with Niño indices, with correlation coefficients
258 of 0.6–0.9 for Niño1+2, Niño3 and Niño3.4 indices and are statistically significant at 95%
259 confidence level. If the lead-lag correlation is based on 1997–2015 when biomass burning data
260 are all derived from satellite observations, the correlations will be higher with the correlation

261 coefficient between Niño1+2 index and BC_{bb} emission rate exceeding 0.95 (Fig. 2c). It suggests
 262 that the biomass burning emissions of BC are enhanced during El Niño events, especially in the
 263 preceding fall season. The Niño1+2 index has the highest correlation with BC_{bb} emission rate,
 264 while Niño4 index has the lowest correlation coefficient, indicating that the Eastern-Pacific
 265 type of El Niño exerts a stronger modulation in BC_{bb} emissions over the MC region than the
 266 Central-Pacific type of El Niño.

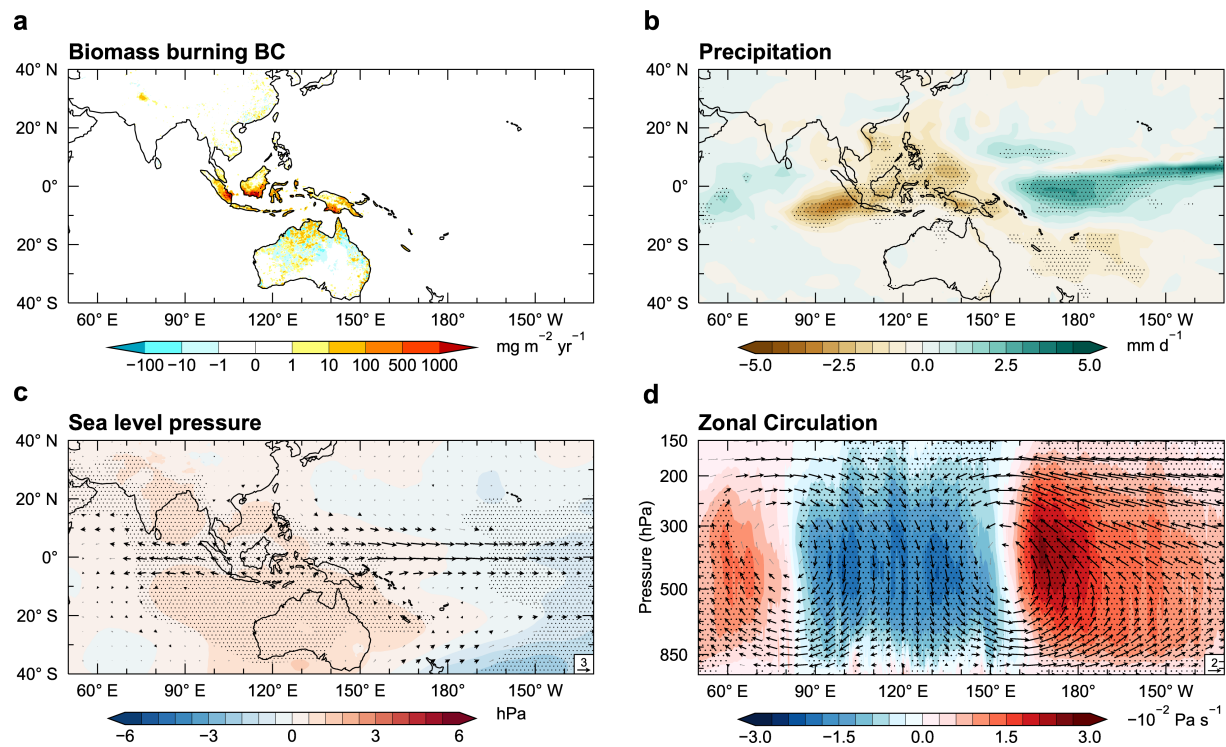


267
 268 **Fig. 2.** Historical relationship between biomass burning black carbon emissions over the Maritime Continent
 269 and El Niño–Southern Oscillation. **a** Seasonal variation of biomass burning black carbon emission rate (Tg
 270 yr⁻¹) over the Maritime Continent during 1950–2015. The shades indicate 1 standard deviation. El Niño years
 271 are 1951, 1953, 1957, 1963, 1965, 1968, 1969, 1972, 1976, 1977, 1982, 1986, 1987, 1991, 1994, 1997, 2002,
 272 2004, 2006, 2009 and 2015. La Niña years are 1950, 1954, 1955, 1956, 1964, 1970, 1971, 1973, 1974, 1975,
 273 1984, 1988, 1995, 1998, 1999, 2000, 2005, 2007, 2008, 2010 and 2011. **b** Lead-lag correlations between the

274 December–January–February mean Niño indices and the biomass burning black carbon emission rate over
 275 the Maritime Continent during 1950–2015. The “−1” and “0” in the x-axis labels represent the preceding and
 276 following year, respectively and the statistically significant correlations (at the 95% level) are marked by
 277 solid markers. **c** Lead-lag correlations the same to **b**, expect the data are during 1997–2015. Biomass burning
 278 black carbon emission data are from BB4CMIP dataset. Niño indices are calculated from ERSSTv5.

279

280 From the perspective of the annual cycle of precipitation climatology, boreal fall is the dry
 281 season in the MC region with relatively little precipitation (Zhang et al., 2016). In general, the
 282 MC is under the ascending branch of the Walker Circulation. However, during the developing
 283 phase of El Niño, the updraft vertical motion is suppressed (Fig. 3d), which coincides with the
 284 increased sea level pressure over the region spanning from the eastern Indian Ocean to the west
 285 Pacific warm pool (Fig. 3c). A weakened convection due to the suppressed updraft decreases
 286 the precipitation over the MC and the eastern Indian Ocean (Fig. 3b). The dry condition over
 287 the MC is favorable for fire occurrence. The increased fires also release more heat, which is
 288 conductive to temperature increase and further worsen the dry conditions. The intensified fire
 289 activities increase BC emissions into the air (Fig. 3a), which are likely to reside in the air for a
 290 longer time under dry conditions (Wu et al., 2013).



291

292 **Fig. 3.** Anomalies in boreal fall season preceding El Niño events compared to the climatology in **a** biomass
 12

293 burning black carbon emission rate ($\text{mg m}^{-2} \text{ yr}^{-1}$), **b** precipitation (mm d^{-1}), **c** sea level pressure (hPa) and
294 10m winds (m s^{-1}), and **d** zonal circulation (reference vector) and pressure velocity (contour, $-10^{-2} \text{ Pa s}^{-1}$).
295 Biomass burning black carbon emission data are from the BB4CMIP dataset. Meteorological parameters are
296 from GPCP and ERA5 reanalysis. The dotted areas indicate statistical significance more than 95% confidence
297 level from a two-tailed Student's *t*-test. The black vectors indicate that the statistical significance of latitudinal
298 winds or meridional (vertical) winds is more than 95% confidence level from a two-tailed Student's *t*-test,
299 while the grey vectors indicate the insignificant winds. The climatology is based on 1950–2015. El Niño
300 years are 1951, 1953, 1957, 1963, 1965, 1968, 1969, 1972, 1976, 1977, 1982, 1986, 1987, 1991, 1994, 1997,
301 2002, 2004, 2006, 2009 and 2015, which are selected by the method of NOAA CPC.

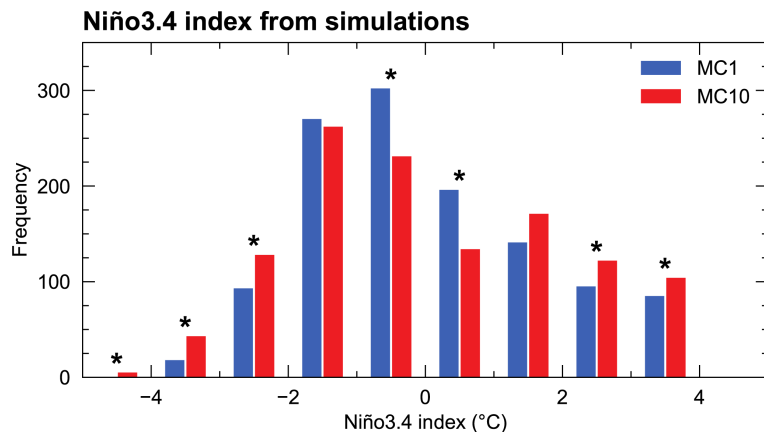
302

303 *b. Biomass burning BC from the Maritime Continent enhances ENSO variability*

304 The analysis above points out that BC emissions from biomass burning over the MC
305 increase during the preceding boreal fall seasons of El Niño events from the perspective of the
306 annual cycle. The strongly increased BC_{bb} can also impact ENSO statistics via its radiative
307 effects. The standard deviation of monthly Niño3.4 index after removing the annual cycle
308 simulated in CESM increases from 1.69 °C in MC1 to 1.92 °C in MC10. It implies that
309 substantial increases in BC emissions from biomass burning over the MC could enhance ENSO
310 variability.

311 Figure 4 shows histograms of the monthly Niño3.4 index obtained from the MC1 and
312 MC10 simulations. The frequency distribution of Niño3.4 index in MC10 is different from that
313 in MC1 based on the Kolmogorov–Smirnov test ($p < 0.01$). The frequencies at the positive and
314 negative tails of the monthly Niño3.4 index significantly increase in MC10, indicating that the
315 increase in BC_{bb} over the MC may enhance the ENSO variability and increase the frequency of
316 extreme ENSO events. If the ENSO years are identified based on the NDJ or DJF mean Niño3.4
317 index, the frequencies extreme El Niño (La Niña) events change from 23 (16) per 100 years in
318 MC1 to 25 (19) per 100 years in MC10.

319

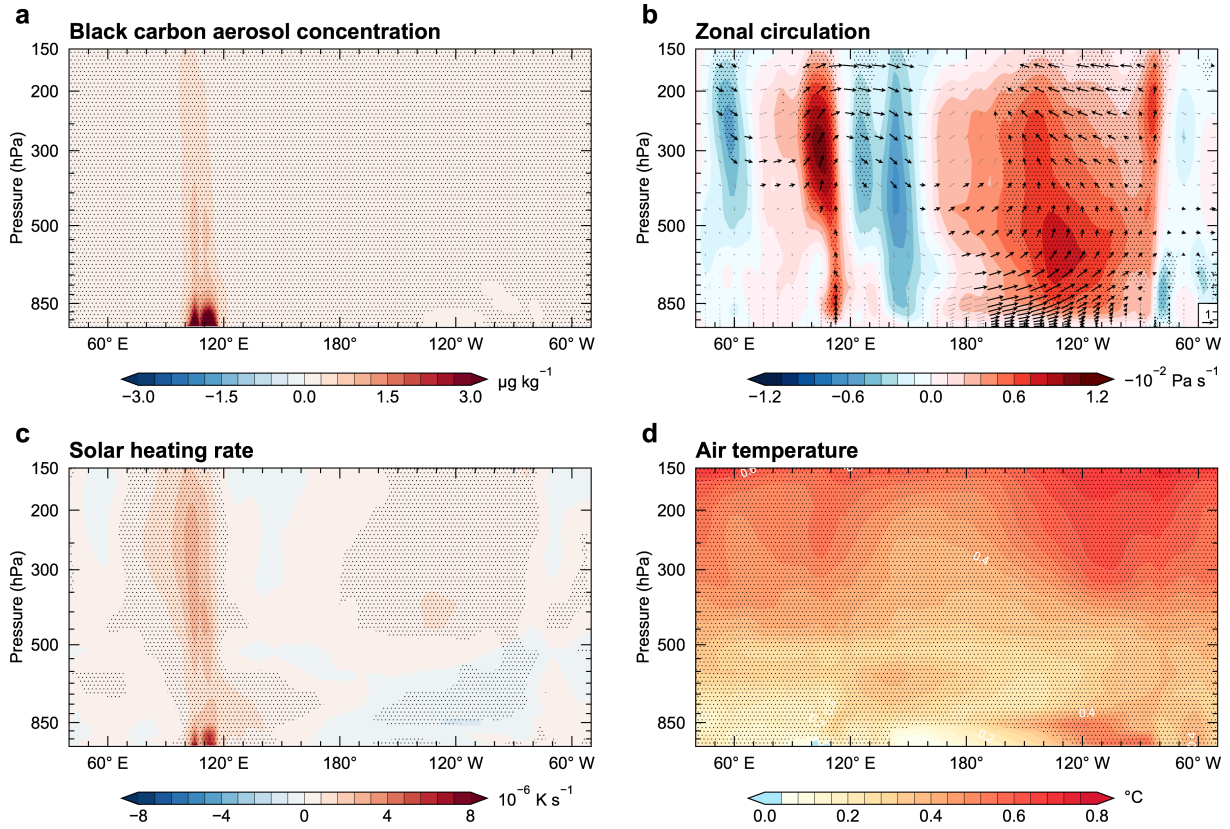


320 **Fig. 4.** Frequency distribution of the monthly Niño3.4 index (°C) of 1200 months from MC1 (blue bars) and
 321 MC10 (red bars). Bars with asterisks indicate statistically significant changes with respect to the upper and
 322 lower 5th percentiles of a probability distribution function for each Niño3.4 index bin derived from a 1400-
 323 year CESM preindustrial simulation.

324

325 *c. Potential mechanisms of BC impacts on ENSO variability*

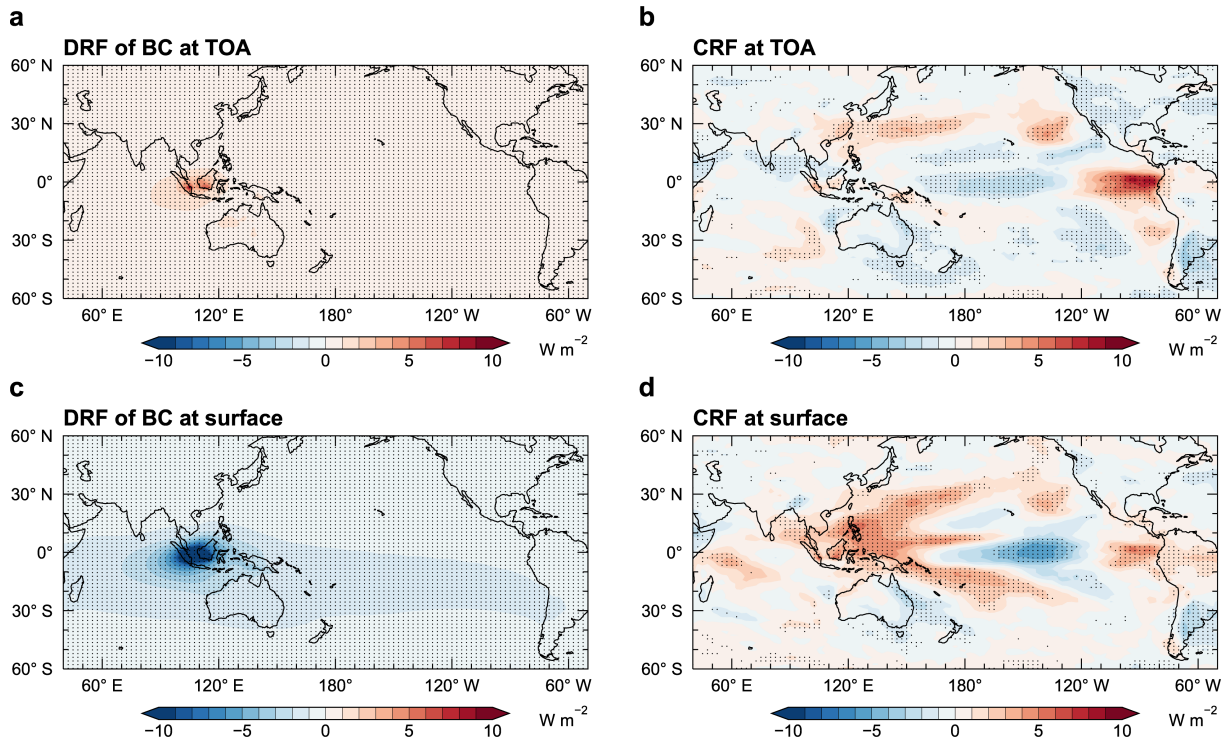
326 Potential mechanisms of how BC_{bb} affects the ENSO variability are examined here. We
 327 investigate the pressure-longitude cross-sections averaged over 3° S– 0° of the difference in BC
 328 concentration, zonal circulation, shortwave heating rate and air temperature in Fig. 5. The
 329 latitude band of 3° S– 0° is chosen because it can better show the BC plume from the high
 330 emission area over the MC (Fig. 1). The ten-fold increase in BC_{bb} emissions in the MC leads to
 331 a strong increase in BC concentrations between 100° E and 120° E near the equator (Fig. 5a).
 332 The maximum increase locates below 850 hPa and it extends to the upper troposphere. As the
 333 most important absorbing aerosol, BC heats the atmosphere through absorbing solar radiation.
 334 With the increase in BC aerosol concentration, the shortwave atmospheric heating rate is
 335 enhanced over the MC (Fig. 5c). While the BC concentration primarily rises in the lower
 336 troposphere, the anomalous shortwave heating exerts a strong influence throughout the entire
 337 atmospheric column, owing to the efficient solar absorption of BC at higher altitudes.
 338 Additionally, the reduction in cloud coverage associated with a dearth of precipitation also
 339 contributes to the shortwave heating.



340 **Fig. 5.** Pressure-longitude cross-sections averaged over 3° S– 0° of differences between the MC1 and MC10
 341 cases for **a** Black carbon aerosol concentration ($\mu\text{g kg}^{-1}$), **b** zonal circulation (reference vector) and vertical
 342 velocity (contour, -10^{-2} Pa s^{-1}), **c** shortwave heating rate (10^{-6} K s^{-1}) and **d** air temperature ($^{\circ}\text{C}$). In **b**, the
 343 red shading indicate rising motion as the contour scale is negative. The differences are calculated from
 344 simulated data by ($V_{\text{annual, MC10}} - V_{\text{annual, MC1}}$). $V_{\text{annual, MC1}}$ is the annual mean of 100 years in MC1 case for each
 345 parameter. The same for $V_{\text{annual, MC10}}$ but in MC10 case. The dotted areas indicate statistical significance more
 346 than 95% confidence level from a two-tailed Student's *t*-test. The black vectors indicate that the statistical
 347 significance of latitudinal winds or vertical winds is more than 95% confidence level from a two-tailed
 348 Student's *t*-test, while the grey vectors indicate the insignificant winds.

349
 350
 351 Over the MC (95° E– 155° E, 10° S– 10° N), the ten-fold increase in BC_{bb} emissions induce
 352 a DRF of 1.3 W m^{-2} at the top of atmosphere (TOA) and of -4.4 W m^{-2} at the surface (Figs. 6a,
 353 6c), showing a strong solar absorption of 5.7 W m^{-2} in the atmosphere. The anomalous heating
 354 in the atmospheric column induces a strong ascending motion above the BC layer between 105°
 355 E and 115° E (Fig. 5b). The enhanced updraft is accompanied by an anomalous subsidence over
 356 120° – 160° E of the tropical Pacific (Fig. 5b), which coincides to the increasing sea level

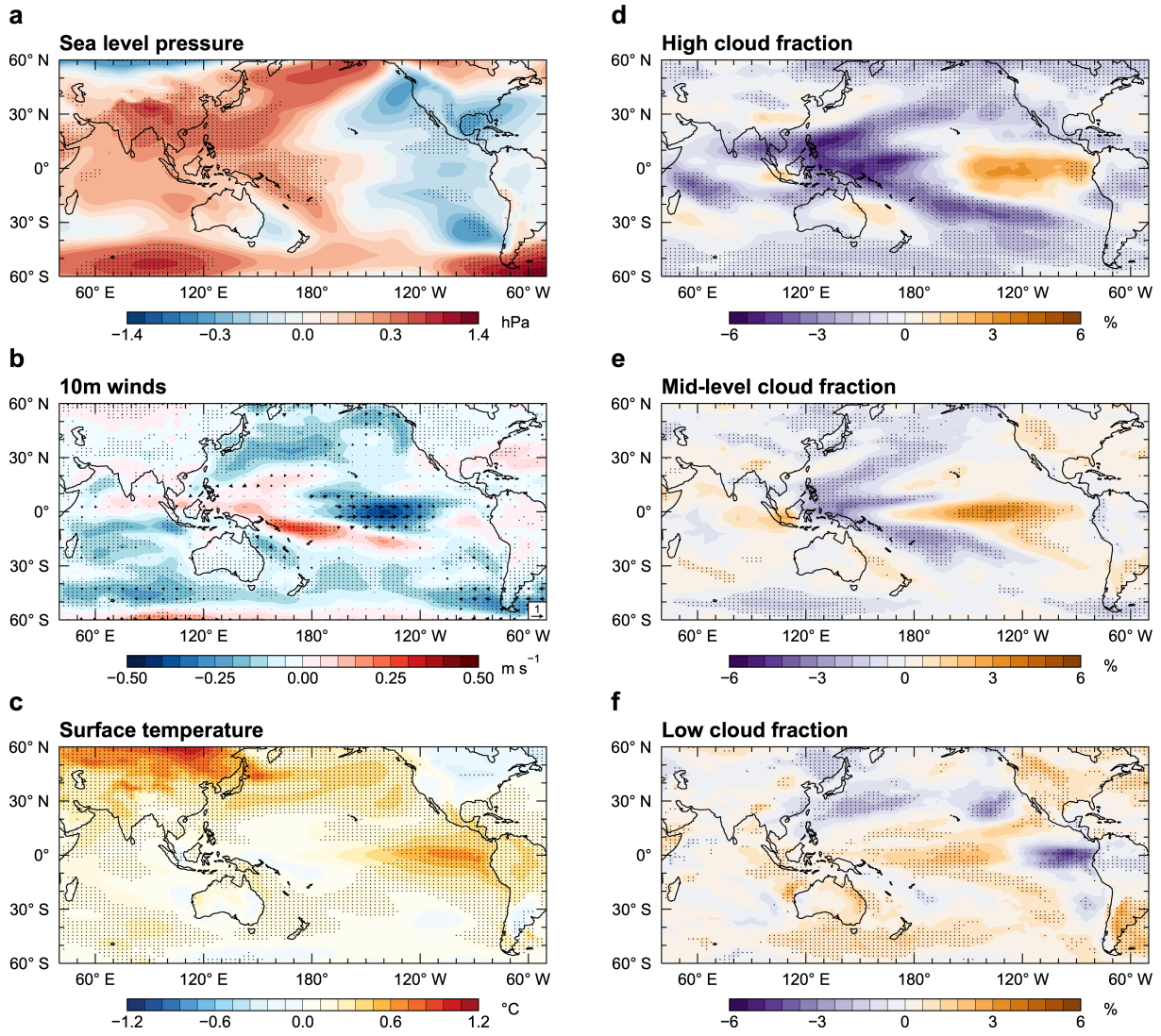
357 pressure over the western Pacific (Fig. 7a). In the lower troposphere over the western Pacific,
358 the subsidence is expected to diverge. One anomalous horizontal branch moves towards east
359 over the central tropical Pacific (Figs. 5b, 7b). Under normal circumstances, the easterly trade
360 winds move the sea surface water from the eastern tropical Pacific to the west. Meanwhile, the
361 upwelling of cold water from the deep sea cools the sea surface over the eastern tropical Pacific,
362 resulting in lower SST in the eastern tropical Pacific than the western Pacific. However, in the
363 MC10 case, the westerly wind anomaly weakens the easterly trade winds, causing a reduced
364 transport of sea surface water from east to west. As a result, the east-west SST gradient is
365 weakened by the substantial increase in BC_{bb} emissions over the MC, leading to the anomalous
366 warming over the eastern tropical Pacific (Figs. 5d, 7c). The anomalous warming of sea surface
367 water causes the anomalous upward motion of the atmosphere around $130^{\circ}W$ (Fig. 5b), leading
368 to a decrease in low cloud fraction and increase in high cloud fraction (Figs. 7d, 7f). In the
369 atmosphere, low clouds mainly scatter solar radiation and pose net cooling effect to the earth
370 system, while high clouds consist chiefly of ice crystals, which can absorb the longwave
371 radiation from the surface and heat the earth. The change in the vertical profile of cloud amount
372 leads to a positive cloud radiative forcing (CRF) over the eastern tropical Pacific (Figs. 6b, 6d),
373 which is also conducive to sea surface warming (Fig. 7c). Over the central Pacific, the
374 increased low clouds and mid-level clouds (Figs. 7e, 7f) induce a negative CRF over this region
375 (Figs. 6b, 6d).



376

377 **Fig. 6.** Differences in radiative effects (W m^{-2}) between the MC1 and MC10 cases, including direct radiative
 378 forcing (DRF) caused by black carbon at **a** the top of atmosphere and **c** the surface as well as net cloud
 379 radiative forcing (CRF) at **b** the top of atmosphere and **d** the surface. The differences are calculated from
 380 simulated data by ($V_{\text{annual, MC10}} - V_{\text{annual, MC1}}$). $V_{\text{annual, MC1}}$ is the annual mean of 100 years in MC1 case for each
 381 parameter. The same for $V_{\text{annual, MC10}}$ but in MC10 case. The dotted areas indicate statistical significance more
 382 than 95% confidence level from a two-tailed Student's *t*-test.

383



384 **Fig. 7.** Differences between MC1 and MC10 cases in **a** sea level pressure (hPa), **b** 10m wind vectors and
385 speeds (m s⁻¹), **c** surface temperature (°C), **d** high cloud fraction (%), **e** mid-level cloud fraction (%) and **f**
386
387 low cloud fraction (%). The differences are calculated from simulated data by ($V_{\text{annual, MC10}} - V_{\text{annual, MC1}}$). $V_{\text{annual,}}$
388 MC1 is the annual mean of 100 years in MC1 case for each parameter. The same for $V_{\text{annual, MC10}}$ but in MC10
389 case. The dotted areas indicate statistical significance more than 95% confidence level from a two-tailed
390 Student's *t*-test. The black vectors indicate that the statistical significance of latitudinal winds or meridional
391 winds is more than 95% confidence level from a two-tailed Student's *t*-test, while the grey vectors indicate
392 the insignificant winds.

393

394 Due to the effects of weakened easterly trade winds and positive CRF, the SST over eastern
395 tropical Pacific in the MC10 case increases significantly relative to the MC1 case, which further
396 enhances ENSO variability and increases the frequency of extreme ENSO events. Wang Y. et
18

397 al. (2019) found that a uniform sea surface warming could increase ENSO amplitudes and the
398 frequency of ENSO events. Previous studies also showed that faster warming in the eastern
399 tropical Pacific than other regions due to westerly wind anomalies in the equatorial Pacific
400 under global warming (Xie et al., 2010) could promote an increase in the frequency of extreme
401 El Niño events (Cai et al., 2014, 2022). It is consistent with this study that the warming over
402 eastern tropical Pacific due to the ten-fold increase in BC_{bb} emissions increases the frequency
403 of extreme El Niño events. Some studies have shown that a La Niña-like change occurs in the
404 mean state of SST across the equatorial Pacific due to the damping effect of upwelling sea water
405 in the eastern equatorial Pacific on the increase of SST (Latif and Keenlyside, 2009; Lian et al.,
406 2018). Cai et al. (2015) argued that a faster warming rate of the MC than the central equatorial
407 Pacific, enhanced upper ocean vertical temperature gradients in the central equatorial Pacific
408 and increased frequency of extreme El Niño events are conducive to development of extreme
409 La Niña events. These support our finding that the frequency of extreme La Niña events is
410 enhanced due to the ten-fold increase in BC_{bb}.

411

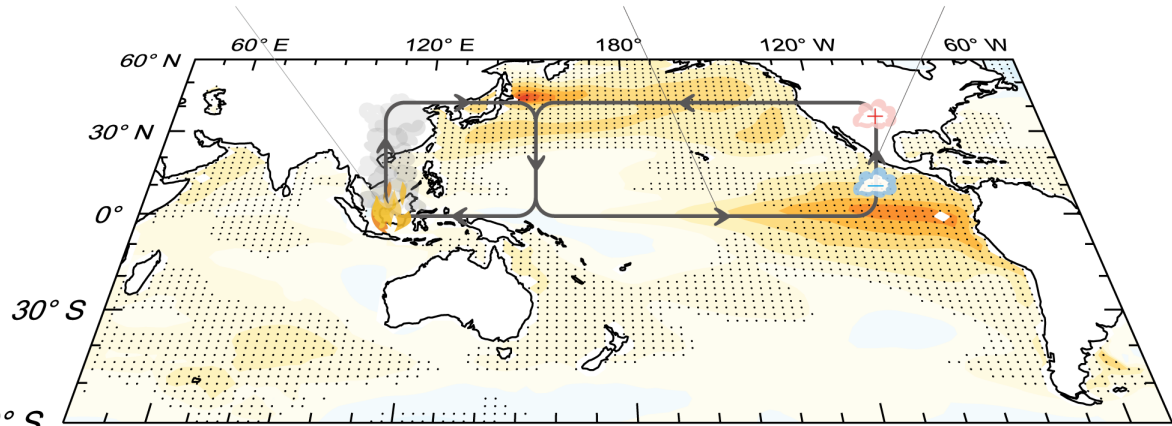
412 **4. Conclusions and discussions**

413 In this study, we investigate the meteorological parameters leading to the increase of BC_{bb}
414 emissions over the MC associated with El Niño and then examine the impact of substantial
415 increases in BC_{bb} emissions on the ENSO variability and the frequency of extreme ENSO
416 events using CESM model sensitivity experiments. The BC_{bb} emission over the MC in the fall
417 season preceding the boreal winter of the mature phase of ENSO events is positively correlated
418 with Niño indices. El Niño can increase the biomass burning emissions over the MC by
419 enhancing the dry conditions. We also show that the Eastern-Pacific type of El Niño exerts a
420 stronger modulation in BC_{bb} emissions over the MC region than the Central-Pacific type of El
421 Niño.

422 A ten-fold increase of BC_{bb} emissions over the MC substantially warms the atmosphere
423 and enhances the ascending air motion above the BC layer over the MC, leading to changes in
424 the atmospheric circulation over the western Pacific. The changed atmospheric circulation
425 further weakens the near-surface easterly trade winds over the central-to-eastern tropical Pacific

426 and weakens the east-west SST gradient, which reduces upwelling of mean cold subsurface
 427 water and leads to an increase in SST over the eastern tropical Pacific. Meanwhile, the low
 428 cloud fraction decreases and the high cloud fraction increases over the eastern tropical Pacific,
 429 which further enhances the increase in SST. When the mean SST increases over the eastern
 430 tropical Pacific, ENSO variability is enhanced and the frequency of extreme El Niño and La
 431 Niña events is increased due to the ten-fold of BC_{bb} emissions over the MC, as simulated in the
 432 CESM experiments. It highlights that there might be more extreme ENSO events if there were
 433 more BC_{bb} emissions from the MC in a warmer future. The mechanism of the impacts of BC_{bb}
 434 aerosol emissions from the MC on ENSO are illustrated in the schematic Fig. 8.

- ① BC aerosols from the fire emissions absorb solar radiation and heat the air, which enhances the updraft over the MC
- ② Westerly anomaly weakens the trade wind and the tropical east-west SST gradient
- ③ Decreased low clouds and increased high clouds further enhance the increase of the SST



435 **Fig. 8.** Mechanism of the impacts of biomass burning black carbon aerosol emissions from the Maritime
 436 Continent on El Niño–Southern Oscillation. Color shadings represent the difference in sea surface
 437 temperature between the MC1 and MC10 cases. Arrows indicates the difference in atmospheric circulation
 438 between the MC1 and MC10 cases. The schematic highlights the tropical Pacific mean state changes in
 439 response to enhanced black carbon emissions over the Maritime Continent. The change in El Niño–Southern
 440 Oscillation statistics can then follow the mean state changes but is likely model dependent.
 441

442
 443 There are some limitations and uncertainties in the study. Concerning the experimental
 444 design for exploring the interaction between BC_{bb} and ENSO, two key factors need to be
 445 considered. Firstly, current models lack the capability of online calculation of BC_{bb} emissions.
 446 Secondly, the oceanic responses are much slower than the atmosphere. On the background of
 447 these factors, the direct response of BC emissions over the MC region to individual El Niño

448 events and the influence of the large increase in BC emissions on ENSO statistical probability
449 due to mean state changes are separately analyzed in this study with different time scales. In
450 the real world, the loop linking the increased BC emissions during an El Niño event back to
451 another ENSO event could be hidden by the internal variability. Besides, any change in extreme
452 ENSO events in the real world is difficult to be attributed to the changing aerosols due to their
453 weak forcing compared to natural variability. To address these challenges, the annual BC_{bb}
454 emissions from the MC region are amplified by a factor of 10 in the CESM simulation (MC10)
455 for investigating the BC impact on ENSO. It allows the signal of climate response to BC to be
456 stronger than internal variability of the climate model, and such a large perturbation was also
457 adopted in previous studies (e.g., Lou et al., 2019a, b; Sand et al., 2013, 2015; Stjern et al.,
458 2017; Yang et al., 2019). However, in the real world, it is unrealistic that BC_{bb} emissions over
459 the MC associated with El Niño alone can reach 10 times of that in 2006, which is a relatively
460 high emission year affected by a moderate El Niño.

461 When conducting model simulations in this study, the atmosphere component focuses on
462 the troposphere with 30 vertical levels from the surface to about 3.6 hPa. However, the biomass
463 burning aerosol can also induce deep convection due to their release of sensible heat and affect
464 stratospheric climate (Trentmann et al., 2006; Chavan et al., 2021). Whether BC emissions from
465 the MC can affect stratospheric climate and feedback on ENSO requires further studies using a
466 high-top atmospheric model.

467 The response of ENSO variability to external climate forcing in model simulations remains
468 a controversial topic, as ENSO is largely influenced by a delicate balance of multiple
469 amplification and damping feedbacks. As indicated in Lou et al. (2019a), the 2-degree version
470 of CESM1.2 simulates more extreme ENSO events than observations. We use the 2-degree
471 atmosphere configuration because the ENSO variability requires long-term simulations and 2-
472 degree atmosphere configuration is much more efficient than 1-degree configuration. Also, the
473 model resolution and version are consistent with our previous study (Lou et al., 2019a),
474 although it may not be the most accurate model version in simulating ENSO statistics. Some
475 modeling studies show weakened ENSO variability under a warming climate (Kohyama et al.,
476 2018), while CESM results showed the opposite (Wang Y. et al., 2019). Therefore, we cannot
477 rule out the model dependence of these simulation results. Also, the 100-year results may not

478 be long enough to fully capture the ENSO statistics. These deserve further exploration with
479 multi-models, large ensemble and long-term simulations in future studies.

480 In this study, we focused on BC emissions from the MC region, but we also note that
481 ENSO modulates fire across the tropics with some influences being potentially constructive and
482 other aspects being destructive, which also requires future investigation.

483 *Acknowledgments.*

484 This research was support by the National Natural Science Foundation of China (grant
485 41975159), Jiangsu Science Fund for Distinguished Young Scholars (grant BK20211541) and
486 the Jiangsu Science Fund for Carbon Neutrality (grant BK20220031). H.W. acknowledges the
487 support by the U.S. Department of Energy (DOE), Office of Science, Office of Biological and
488 Environmental Research (BER), as part of the Earth and Environmental System Modeling
489 program. The Pacific Northwest National Laboratory (PNNL) is operated for DOE by Battelle
490 Memorial Institute under contract DE-AC05-76RLO1830.

491

492 *Data Availability Statement.*

493 The emission data (i.e., BB4CMIP, CEDS) are available from <https://esgf-node.llnl.gov/search/input4mips/>. ERSST v5 sea surface temperature data are available from
494 <https://psl.noaa.gov/data/gridded/data.noaa.ersst.v5.html>. ERA5 reanalysis data are available
495 from <https://cds.climate.copernicus.eu/>. GPCP precipitation data are available from
496 <https://www.ncei.noaa.gov/data/global-precipitation-climatology-project-gpcp-monthly/access/>. SST data from a 1400-year CESM preindustrial control simulation are
497 available from
498 https://www.earthsystemgrid.org/dataset/ucar.cgd.ccsm4.b.e11.B1850C5CN.f19_g16.008.atm.proc.monthly_ave.TS.html. The processed modeling data are available at
499 <https://doi.org/10.5281/zenodo.7312877>.

REFERENCES

504 Adler, R. F., and Coauthors, 2018: The Global Precipitation Climatology Project (GPCP)
505 Monthly Analysis (New Version 2.3) and a Review of 2017 Global Precipitation.
506 *Atmosphere*, **9**, 138, <https://doi.org/10.3390/atmos9040138>.

507 Bjerknes, J., 1969: Atmospheric teleconnections from the equatorial Pacific. *Mon. Wea. Rev.*,
508 **97**, 163–172, [https://doi.org/10.1175/1520-0493\(1969\)097<0163:ATFTEP>2.3.CO;2](https://doi.org/10.1175/1520-0493(1969)097<0163:ATFTEP>2.3.CO;2).

509 Cai, W., and Coauthors, 2014: Increasing frequency of extreme El Niño events due to
510 greenhouse warming. *Nat. Clim. Chang.*, **4**, 111–116,
511 <https://doi.org/10.1038/nclimate2100>.

512 —, and Coauthors, 2015: Increased frequency of extreme La Niña events under greenhouse
513 warming. *Nat. Clim. Chang.*, **5**, 132–137, <https://doi.org/10.1038/nclimate2492>.

514 —, and Coauthors, 2018: Increased variability of eastern Pacific El Niño under greenhouse
515 warming. *Nature*, **564**, 201–206, <https://doi.org/10.1038/s41586-018-0776-9>.

516 —, B. Ng, G. Wang, A. Santoso, L. Wu, and K. Yang, 2022: Increased ENSO sea surface
517 temperature variability under four IPCC emission scenarios. *Nat. Clim. Chang.*, **12**, 228–
518 231, <https://doi.org/10.1038/s41558-022-01282-z>.

519 Carlson, K. M., and Coauthors, 2012: Committed carbon emissions, deforestation, and
520 community land conversion from oil palm plantation expansion in West Kalimantan,
521 Indonesia. *Proc. Natl. Acad. Sci. U.S.A.*, **109**, 7559–7564,
522 <https://doi.org/10.1073/pnas.1200452109>.

523 Chandra, S., J. R. Ziemke, B. N. Duncan, T. L. Diehl, N. J. Livesey, and L. Froidevaux, 2009:
524 Effects of the 2006 El Niño on tropospheric ozone and carbon monoxide: implications for
525 dynamics and biomass burning. *Atmos. Chem. Phys.*, **9**, 4239–4249,
526 <https://doi.org/10.5194/acp-9-4239-2009>.

527 Chavan, P., S. Fadnavis, T. Chakraborty, C. E. Sioris, S. Griessbach, and R. Müller, 2021: The
528 outflow of Asian biomass burning carbonaceous aerosol into the upper troposphere and
529 lower stratosphere in spring: radiative effects seen in a global model. *Atmos. Chem. Phys.*,
530 **21**, 14371–14384, <https://doi.org/10.5194/acp-21-14371-2021>.

531 Chen, Y., D. C. Morton, N. Andela, G. R. van der Werf, L. Giglio, and J. T. Randerson, 2017:
532 A pan-tropical cascade of fire driven by El Niño/Southern Oscillation. *Nat. Clim. Chang.*,

533 7, 906–911, <https://doi.org/10.1038/s41558-017-0014-8>.

534 Dennis, R. A., and Coauthors, 2005: Fire, people and pixels: Linking social science and remote
535 sensing to understand underlying causes and impacts of fires in Indonesia. *Hum. Ecol.*, **33**,
536 465–504, <https://doi.org/10.1007/s10745-005-5156-z>.

537 Duncan, B. N., I. Bey, M. Chin, L. J. Mickley, T. D. Fairlie, R. V. Martin, and H. Matsueda,
538 2003: Indonesian wildfires of 1997: Impact on tropospheric chemistry. *J. Geophys. Res.*
539 *Atmos.*, **108**, 4458, <https://doi.org/10.1029/2002JD003195>.

540 Fasullo, J. T., N. Rosenbloom, and R. Buchholz, 2023: A multiyear tropical Pacific cooling
541 response to recent Australian wildfires in CESM2. *Sci. Adv.*, **9**, eadg1213,
542 <https://doi.org/10.1126/sciadv.adg1213>.

543 Hersbach, H., and Coauthors, 2020: The ERA5 global reanalysis. *Q.J.R. Meteorol. Soc.*, **146**,
544 1999–2049, <https://doi.org/10.1002/qj.3803>.

545 Hoesly, R. M., and Coauthors, 2018: Historical (1750–2014) anthropogenic emissions of
546 reactive gases and aerosols from the Community Emissions Data System (CEDS). *Geosci.*
547 *Model Dev.*, **11**, 369–408, <https://doi.org/10.5194/gmd-11-369-2018>.

548 Hu, C., S. Yang, Q. Wu, Z. Li, J. Chen, K. Deng, T. Zhang, and C. Zhang, 2016: Shifting El
549 Niño inhibits summer Arctic warming and Arctic sea-ice melting over the Canada Basin.
550 *Nat. Commun.*, **7**, 11721, <https://doi.org/10.1038/ncomms11721>.

551 Hurrell, J. W., and Coauthors, 2013: The Community Earth System Model: a framework for
552 collaborative research. *Bull. Am. Meteorol. Soc.*, **94**, 1339–1360,
553 <https://doi.org/10.1175/BAMS-D-12-00121.1>.

554 Iizumi, T., J.-J. Luo, A. J. Challinor, G. Sakurai, M. Yokozawa, H. Sakuma, M. E. Brown, and
555 T. Yamagata, 2014: Impacts of El Niño Southern Oscillation on the global yields of major
556 crops. *Nat. Commun.*, **5**, 3712, <https://doi.org/10.1038/ncomms4712>.

557 Jiménez-Muñoz, J. C., C. Mattar, J. Barichivich, A. Santamaría-Artigas, K. Takahashi, Y. Malhi,
558 J. A. Sobrino, and G. van der Schrier, 2016: Record-breaking warming and extreme
559 drought in the Amazon rainforest during the course of El Niño 2015–2016. *Sci. Rep.*, **6**,
560 33130, <https://doi.org/10.1038/srep33130>.

561 Kang, S., Y. Zhang, Y. Qian, and H. Wang, 2020: A review of black carbon in snow and ice and
562 its impact on the cryosphere. *Earth Sci. Rev.*, **210**, 103346,
25

563 <https://doi.org/10.1016/j.earscirev.2020.103346>.

564 Kim, M.-K., W. K. M. Lau, K.-M. Kim, J. Sang, Y.-H. Kim, and W.-S. Lee, 2016: Amplification
565 of ENSO effects on Indian summer monsoon by absorbing aerosols. *Clim. Dyn.*, **46**, 2657–
566 2671, <https://doi.org/10.1007/s00382-015-2722-y>.

567 Kohyama, T., D. L. Hartmann, and D. S. Battisti, 2018: Weakening of Nonlinear ENSO Under
568 Global Warming. *Geophys. Res. Lett.*, **45**, 8557–8567,
569 <https://doi.org/10.1029/2018GL079085>.

570 Lack, D. A., and C. D. Cappa, 2010: Impact of brown and clear carbon on light absorption
571 enhancement, single scatter albedo and absorption wavelength dependence of black carbon.
572 *Atmos. Chem. Phys.*, **10**, 4207–4220, <https://doi.org/10.5194/acp-10-4207-2010>.

573 Latif, M., and N. S. Keenlyside, 2009: El Niño/Southern Oscillation response to global warming.
574 *Proc. Natl. Acad. Sci. U.S.A.*, **106**, 20578–20583,
575 <https://doi.org/10.1073/pnas.0710860105>.

576 Lee, H.-H., R. Z. Bar-Or, and C. Wang, 2017: Biomass burning aerosols and the low-visibility
577 events in Southeast Asia. *Atmos. Chem. Phys.*, **17**, 965–980, <https://doi.org/10.5194/acp-17-965-2017>.

579 Lian, T., D. Chen, J. Ying, and Y. Tang, 2018: The evolving ENSO observing system. *National
580 Science Review*, **5**, 805–807, <https://doi.org/10.1093/nsr/nwy137>.

581 Liu, X., and Coauthors, 2012: Toward a minimal representation of aerosols in climate models:
582 description and evaluation in the Community Atmosphere Model CAM5. *Geosci. Model
583 Dev.*, **5**, 709–739, <https://doi.org/10.5194/gmd-5-709-2012>.

584 —, P.-L. Ma, H. Wang, S. Tilmes, B. Singh, R. C. Easter, S. J. Ghan, and P. J. Rasch, 2016:
585 Description and evaluation of a new four-mode version of the Modal Aerosol Module
586 (MAM4) within version 5.3 of the Community Atmosphere Model. *Geosci. Model Dev.*,
587 **9**, 505–522, <https://doi.org/10.5194/gmd-9-505-2016>.

588 Lou, S., Y. Yang, H. Wang, J. Lu, S. J. Smith, F. Liu, and P. J. Rasch, 2019a: Black carbon
589 increases frequency of extreme ENSO events. *J. Clim.*, **32**, 8323–8333,
590 <https://doi.org/10.1175/JCLI-D-19-0549.1>.

591 —, —, —, S. J. Smith, Y. Qian, and P. J. Rasch, 2019b: Black carbon amplifies haze
592 over the North China Plain by weakening the East Asian winter monsoon. *Geophys. Res.*

593 *Lett.*, **46**, 452–460, <https://doi.org/10.1029/2018GL080941>.

594 Marlier, M. E., and Coauthors, 2015a: Regional air quality impacts of future fire emissions in
595 Sumatra and Kalimantan. *Environ. Res. Lett.*, **10**, 054010, <https://doi.org/10.1088/1748-9326/10/5/054010>.

596 ———, R. S. DeFries, P. S. Kim, S. N. Koplitz, D. J. Jacob, L. J. Mickley, and S. S. Myers, 2015b:
597 Fire emissions and regional air quality impacts from fires in oil palm, timber, and logging
598 concessions in Indonesia. *Environ. Res. Lett.*, **10**, 085005, <https://doi.org/10.1088/1748-9326/10/8/085005>.

600 Mcfarquhar, G. M., and H. Wang, 2006: Effects of aerosols on trade wind cumuli over the
601 Indian Ocean: Model simulations. *Q.J.R. Meteorol. Soc.*, **132**, 821–843,
602 <https://doi.org/10.1256/qj.04.179>.

603 Nicolas, J. P., and Coauthors, 2017: January 2016 extensive summer melt in West Antarctica
604 favoured by strong El Niño. *Nat. Commun.*, **8**, 15799,
605 <https://doi.org/10.1038/ncomms15799>.

606 Novakov, T., S. Menon, T. W. Kirchstetter, D. Koch, and J. E. Hansen, 2005: Aerosol organic
607 carbon to black carbon ratios: Analysis of published data and implications for climate
608 forcing. *J. Geophys. Res.*, **110**, D21205, <https://doi.org/10.1029/2005JD005977>.

609 Ramanathan, V., and G. Carmichael, 2008: Global and regional climate changes due to black
610 carbon. *Nat. Geosci.*, **1**, 221–227, <https://doi.org/10.1038/ngeo156>.

611 Rashid, M., S. Yunus, R. Mat, S. Baharun, and P. Lestari, 2014: PM₁₀ black carbon and ionic
612 species concentration of urban atmosphere in Makassar of South Sulawesi Province,
613 Indonesia. *Atmos. Pollut. Res.*, **5**, 610–615, <https://doi.org/10.5094/APR.2014.070>.

614 Sand, M., T. K. Berntsen, Ø. Seland, and J. E. Kristjánsson, 2013: Arctic surface temperature
615 change to emissions of black carbon within Arctic or midlatitudes. *J. Geophys. Res. Atmos.*,
616 **118**, 7788–7798, <https://doi.org/10.1002/jgrd.50613>.

617 ———, T. Iversen, P. Bohlinger, A. Kirkevåg, I. Seierstad, Ø. Seland, and A. Sorteberg, 2015: A
618 Standardized Global Climate Model Study Showing Unique Properties for the Climate
619 Response to Black Carbon Aerosols. *J. Clim.*, **28**, 2512–2526,
620 <https://doi.org/10.1175/JCLI-D-14-00050.1>.

621 Santoso, A., M. J. Mcphaden, and W. Cai, 2017: The defining characteristics of ENSO extremes

623 and the strong 2015/2016 El Niño. *Rev. Geophys.*, **55**, 1079–1129,
624 <https://doi.org/10.1002/2017RG000560>.

625 Sattar, Y., M. Rashid, M. Ramli, and B. Sabariah, 2014: Black carbon and elemental
626 concentration of ambient particulate matter in Makassar Indonesia. *IOP Conf. Ser.: Earth
627 Environ. Sci.*, **18**, 012099, <https://doi.org/10.1088/1755-1315/18/1/012099>.

628 Schwarz, J. P., and Coauthors, 2008: Measurement of the mixing state, mass, and optical size
629 of individual black carbon particles in urban and biomass burning emissions. *Geophys.
630 Res. Lett.*, **35**, L13810, <https://doi.org/10.1029/2008GL033968>.

631 Sobel, A. H., and E. D. Maloney, 2000: Effect of ENSO and the MJO on western North Pacific
632 tropical cyclones. *Geophys. Res. Lett.*, **27**, 1739–1742,
633 <https://doi.org/10.1029/1999GL011043>.

634 Stevenson, S. L., 2012: Significant changes to ENSO strength and impacts in the twenty-first
635 century: Results from CMIP5. *Geophys. Res. Lett.*, **39**,
636 <https://doi.org/10.1029/2012GL052759>.

637 Stjern, C. W., and Coauthors, 2017: Rapid Adjustments Cause Weak Surface Temperature
638 Response to Increased Black Carbon Concentrations: Rapid Adjustments Cause Weak BC
639 Response. *J. Geophys. Res. Atmos.*, **122**, 11,462-11,481,
640 <https://doi.org/10.1002/2017JD027326>.

641 Stocker, T., D. Qin, et al. eds., 2013: Frequently Asked Questions. *Climate Change 2013: The
642 Physical Science Basis*. WMO, UNEP, pp. 147,
643 https://www.ipcc.ch/site/assets/uploads/2018/03/WG1AR5_SummaryVolume_FINAL.pdf
644 f.

645 Szopa, S., V. Naik, B. Adhikary, P. Artaxo, T. Berntsen, W.D. Collins, S. Fuzzi, L. Gallardo, A.
646 Kiendler-Scharr, Z. Klimont, H. Liao, N. Unger, P. Zanis et al., 2021: Short-Lived Climate
647 Forcers. In *Climate Change 2021: The Physical Science Basis*. Cambridge University
648 Press, Cambridge, United Kingdom and New York, NY, USA, pp. 817–922,
649 <https://doi.org/10.1017/9781009157896.008>.

650 Thirumalai, K., P. N. DiNezio, Y. Okumura, and C. Deser, 2017: Extreme temperatures in
651 Southeast Asia caused by El Niño and worsened by global warming. *Nat. Commun.*, **8**,
652 15531, <https://doi.org/10.1038/ncomms15531>.

653 Tosca, M. G., J. T. Randerson, C. S. Zender, M. G. Flanner, and P. J. Rasch, 2010: Do biomass
654 burning aerosols intensify drought in equatorial Asia during El Niño? *Atmos. Chem. Phys.*,
655 **10**, 3515–3528, <https://doi.org/10.5194/acp-10-3515-2010>.

656 Trentmann, J., G. Luderer, T. Winterrath, M. D. Fromm, R. Servranckx, C. Textor, M. Herzog,
657 and M. O. Andreae, 2006: Modeling of biomass smoke injection into the lower
658 stratosphere by a large forest fire (Part I): reference simulation. *Atmos. Chem. Phys.*, **6**,
659 5247–5260, <https://doi.org/10.5194/acp-6-5247-2006>.

660 van Marle, M. J. E., and Coauthors, 2017: Historic global biomass burning emissions for
661 CMIP6 (BB4CMIP) based on merging satellite observations with proxies and fire models
662 (1750–2015). *Geosci. Model Dev.*, **10**, 3329–3357, <https://doi.org/10.5194/gmd-10-3329-2017>.

663

664 Wang, B., X. Luo, Y.-M. Yang, W. Sun, M. A. Cane, W. Cai, S.-W. Yeh, and J. Liu, 2019:
665 Historical change of El Niño properties sheds light on future changes of extreme El Niño.
666 *Proc. Natl. Acad. Sci. U.S.A.*, **116**, 22512–22517,
667 <https://doi.org/10.1073/pnas.1911130116>.

668 Wang, C., 2007: Impact of direct radiative forcing of black carbon aerosols on tropical
669 convective precipitation. *Geophys. Res. Lett.*, **34**, L05709,
670 <https://doi.org/10.1029/2006GL028416>.

671 Wang, T., D. Guo, Y. Gao, H. Wang, F. Zheng, Y. Zhu, J. Miao, and Y. Hu, 2018: Modulation
672 of ENSO evolution by strong tropical volcanic eruptions. *Clim. Dyn.*, **51**, 2433–2453,
673 <https://doi.org/10.1007/s00382-017-4021-2>.

674 Wang, Y., Y. Luo, J. Lu, and F. Liu, 2019: Changes in ENSO amplitude under climate warming
675 and cooling. *Clim. Dyn.*, **52**, 1871–1882, <https://doi.org/10.1007/s00382-018-4224-1>.

676 Ward, B., F. S. R. Pausata, and N. M. Maher, 2021: The sensitivity of the El Niño–Southern
677 Oscillation to volcanic aerosol spatial distribution in the MPI Grand Ensemble. *Earth Syst.*
678 *Dyn.*, **12**, 975–996, <https://doi.org/10.5194/esd-12-975-2021>.

679 Ward, P. J., M. Kummu, and U. Lall, 2016: Flood frequencies and durations and their response
680 to El Niño Southern Oscillation: Global analysis. *J. Hydrol.*, **539**, 358–378,
681 <https://doi.org/10.1016/j.jhydrol.2016.05.045>.

682 Wu, R., Z. Wen, and Z. He, 2013: ENSO Contribution to Aerosol Variations over the Maritime

683 Continent and the Western North Pacific during 2000–10. *J. Clim.*, **26**, 6541–6560,
684 <https://doi.org/10.1175/JCLI-D-12-00253.1>.

685 Xie, S.-P., C. Deser, G. A. Vecchi, J. Ma, H. Teng, and A. T. Wittenberg, 2010: Global Warming
686 Pattern Formation: Sea Surface Temperature and Rainfall. *J. Clim.*, **23**, 966–986,
687 <https://doi.org/10.1175/2009JCLI3329.1>.

688 Xu, L., and J.-Y. Yu, 2019: An ENSO-induced aerosol dipole in the west-central Pacific and its
689 potential feedback to ENSO evolution. *Clim. Dyn.*, **52**, 5115–5125,
690 <https://doi.org/10.1007/s00382-018-4435-5>.

691 Yang, Y., and Coauthors, 2016a: Impacts of ENSO events on cloud radiative effects in
692 preindustrial conditions: Changes in cloud fraction and their dependence on interactive
693 aerosol emissions and concentrations. *J. Geophys. Res. Atmos.*, **121**, 6321–6335,
694 <https://doi.org/10.1002/2015JD024503>.

695 —, L. M. Russell, S. Lou, M. A. Lamjiri, Y. Liu, B. Singh, and S. J. Ghan, 2016b: Changes
696 in Sea Salt Emissions Enhance ENSO Variability. *J. Clim.*, **29**, 8575–8588,
697 <https://doi.org/10.1175/JCLI-D-16-0237.1>.

698 —, H. Wang, S. J. Smith, P.-L. Ma, and P. J. Rasch, 2017: Source attribution of black carbon
699 and its direct radiative forcing in China. *Atmos. Chem. Phys.*, **17**, 4319–4336,
700 <https://doi.org/10.5194/acp-17-4319-2017>.

701 —, S. J. Smith, H. Wang, C. M. Mills, and P. J. Rasch, 2019: Variability, timescales, and
702 nonlinearity in climate responses to black carbon emissions. *Atmos. Chem. Phys.*, **19**,
703 2405–2420, <https://doi.org/10.5194/acp-19-2405-2019>.

704 —, L. Zeng, H. Wang, P. Wang, and H. Liao, 2023: Climate effects of future aerosol
705 reductions for achieving carbon neutrality in China. *Sci. Bull.*, **68**, 902–905,
706 <https://doi.org/10.1016/j.scib.2023.03.048>.

707 Zhang, T., S. Yang, X. Jiang, and P. Zhao, 2016: Seasonal–interannual variation and prediction
708 of wet and dry season rainfall over the Maritime Continent: Roles of ENSO and monsoon
709 circulation. *J. Clim.*, **29**, 3675–3695, <https://doi.org/10.1175/JCLI-D-15-0222.1>.